Tuning the electronic and magnetic states of Ca_2RuO_4 with proton evolution

Di Tian,[1,*] Ludi Miao,[2,3,*] Liang Si,[4,5,*] Nathaniel J. Schreiber,[6] Shengchun Shen,[1] Jianbing Zhang,[1] Xinyu Shu,[1] Xiaochao Wang,[4] Hari P. Nair,[6] Jacob P. Ruf,[2] Darrell G. Schlom,[6,7,8,†] Kyle M. Shen,[2,7,‡] and Pu Yu[1,9,§]

[1]*State Key Laboratory of Low Dimensional Quantum Physics and Department of Physics, Tsinghua University, 100084 Beijing, China*
[2]*Department of Physics, Laboratory of Atomic and Solid State Physics, Cornell University, Ithaca, New York 14853, USA*
[3]*Department of Physics, New Mexico State University, Las Cruces, New Mexico 88003, USA*
[4]*School of Physics, Northwest University, Xi'an 710127, China*
[5]*Institut für Festkörperphysik, TU Wien, 1040 Vienna, Austria*
[6]*Department of Materials Science and Engineering, Cornell University, Ithaca, New York 14853, USA*
[7]*Kavli Institute at Cornell for Nanoscale Science, Ithaca, New York 14853, USA*
[8]*Leibniz-Institut für Kristallzüchtung, Max-Born-Str. 2, 12489 Berlin, Germany*
[9]*Frontier Science Center for Quantum Information, 100084 Beijing, China*

(Received 11 October 2023; accepted 29 June 2024; published 22 July 2024)

With strong correlations between lattice, spin, and charge degrees of freedom, the layered ruthenate Ca_2RuO_4 has attracted considerable interest over the past few decades due to its metal-insulator transition, antiferromagnetic-to-ferromagnetic transition, metamagnetic transition, and orbital ordering. Much effort has been devoted to manipulating its crystalline structure through epitaxial strain, chemical substitution, and pressure to clarify the underlying many-body physics and related quantum critical phenomena. Here we report a comprehensive proton intercalation study of Ca_2RuO_4 thin films and investigate their magneto-transport properties arising from structural deformations and carrier doping. It reveals a rich phase diagram with distinct electronic and magnetic ground states. Specifically, with increasing gate voltage during ionic liquid gating, the film first evolves from an insulating state into a metallic state and then gradually turns towards an exotic Mott insulator. Furthermore, we observed an emergent metamagnetic transition from a canted antiferromagnetic to a nearly ferromagnetic state, a characteristic feature conventionally triggered by external magnetic field, but here with electron doping. Our first-principles calculations reveal that these unexpected features could be attributed to the proton evolution-induced synergistic structural distortion and electron doping during ionic liquid gating. Our findings highlight the important role of both lattice and charge degrees of freedom in the intriguing electronic states of Ca_2RuO_4 and provide an effective approach to uncover different properties in quantum materials.

DOI: 10.1103/PhysRevMaterials.8.074408

I. INTRODUCTION

Ca_2RuO_4 has been the subject of intense research interest over the last few decades initially due to its crystalline similarity with Sr_2RuO_4, the first non-copper-layered perovskite superconductor [1]. Being different from Sr_2RuO_4 with an ideal K_2NiF_4 structure, Ca_2RuO_4 hosts orthorhombic distortions featured by additional rotations and tilting of the RuO_6 octahedra [2], as shown in Fig. 1(a). These structural distortions, which are attributed to the smaller ionic radius of Ca^{2+} as compared to Sr^{2+}, lead to stronger electronic correlations as well as larger crystal field splittings within the t_{2g} orbitals. Consequently, the electronic band structure in Ca_2RuO_4 is remarkably modified so that its ground state becomes an antiferromagnetic (AFM) Mott insulator [2,3], in stark contrast to the unconventional superconducting state in Sr_2RuO_4. Excitingly, the strong interplays between the spin, lattice, and charge degrees of freedom in Ca_2RuO_4 give rise to exotic behavior including orbital ordering [4,5], magnons with Higgs mode [6,7], metal-to-insulator transitions [2,8], nonlinear optical response [9,10], and a metamagnetic (MM) transition [11–14]. On top of that, it is expected that the ground state of Ca_2RuO_4 is very sensitive to external structural manipulation, providing a great opportunity to investigate the evolution of corresponding quantum correlated phenomena. For example, both electronic and magnetic properties of Ca_2RuO_4 have been successfully tuned through applications of chemical substitution [15–19], pressure [20–22], and epitaxial strain [23–25].

These fascinating phenomena clarify the critical role of the lattice degree of freedom (lattice distortion) for the electronic and magnetic states in Ca_2RuO_4 Nonetheless, it remains largely unexplored how the charge degree of freedom (i.e., electron doping) would influence these corresponding properties through both the intrinsic band filling and the coupling with other degrees of freedom. Besides, to unveil the complicated interactions in this Mott system, it is of fundamental importance to reveal how the electronic states would evolve

*These authors equally contributed to this work.
†Contact author: schlom@cornell.edu
‡Contact author: kmshen@cornell.edu
§Contact author: yupu@tsinghua.edu.cn

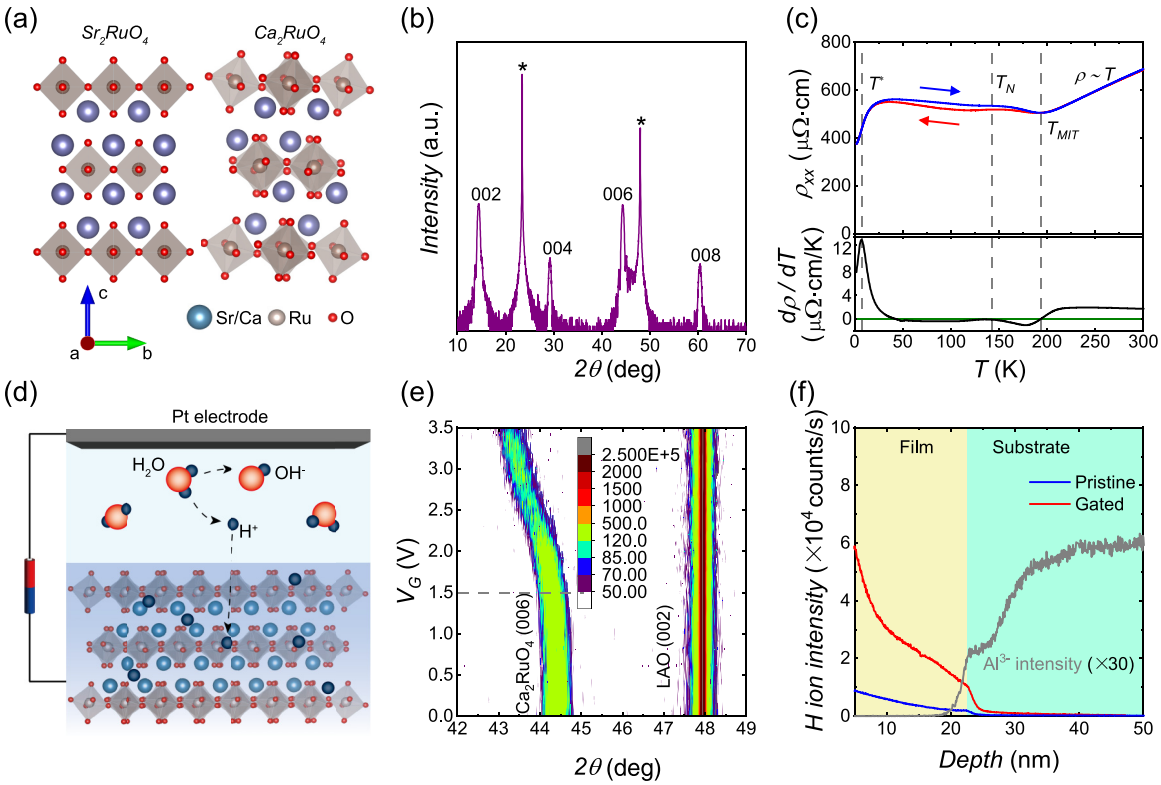

FIG. 1. Proton evolution through ionic liquid gating in Ca_2RuO_4 thin films. (a) Schematic illustration of the crystalline structures of Sr_2RuO_4 and Ca_2RuO_4. The structures are viewed along the pseudocubic [100] direction. (b) XRD spectra of Ca_2RuO_4 thin film grown on a $LaAlO_3$ substrate. The diffraction peaks for LAO substrate are denoted by asterisks. (c) Temperature dependence of longitudinal resistivity ρ_{xx} (upper panel) and corresponding differential curve ($d\rho/dT$, lower panel) measured on a pristine Ca_2RuO_4 film. The dashed lines indicate three characteristic temperatures. For ρ_{xx}, the blue and red lines denote the sweep directions of temperature. (d) Schematic illustration of the experimental setup for the ionic-liquid gating induced proton evolution. (e) Evolution of the Ca_2RuO_4 (006) diffraction peak as a function of gating voltage (V_G) during the ionic liquid gating. During ionic liquid gating the XRD peak position moves from 44.4° to 43.2° due to the proton-intercalation-induced chemical expansion. (f) Measurements of the hydrogen concentrations from both pristine and gated (at 3.5 V) Ca_2RuO_4 films. The intensity of Al^{3+} was used to identify the position of interface between the film and the substrate.

with band filling, which might lead to the discovery of unconventional phase transitions. However, this previously faced a grand challenge to pursue due to the lack of effective methods to achieve pronounced charge doping into these Ru oxides. For instance, although substitution of Ca with La or Pr can achieve electron doping, the doping level is relatively low, and a complete phase diagram upon electron doping still remains elusive [26–28]. Fortunately, recent studies have demonstrated that the magnetic and electronic state of the perovskite ruthenates $SrRuO_3$ and $CaRuO_3$ can be modified through ionic liquid gating (ILG) [29–31] and hydrogen spillover [32], where the ILG-induced proton intercalation introduces substantial electron doping and structural modifications, leading to the exotic magnetic transitions. Therefore, we were able to address the issue about the evolution of the electronic states of Ca_2RuO_4 along with charge doping. Specifically, we studied how the evolution of the t_{2g} orbital occupation is correlated with the electronic and magnetic properties of Ca_2RuO_4, which has been a longstanding elusive issue [33–43].

In this paper we carried out a comprehensive ILG study and detailed first-principles calculations on Ca_2RuO_4 thin films to trace its corresponding electronic and magnetic transitions through *in situ* structural and magneto-transport measurements. Pristine Ca_2RuO_4 under compressive strain is metallic with a canted AFM order at low temperature. With ILG, its conductivity is first enhanced and then significantly decreased and eventually turned into an insulating state that has not been previously observed in a perovskite ruthenate to the best of our knowledge. Furthermore, the magnetic ground state of ILG-Ca_2RuO_4 holds great similarity with pristine Ca_2RuO_4 under high magnetic field, which indicates an ILG-induced MM transition in this system. Theoretical calculations reveal that these exotic states could be understood as the synergistic evolutions of both electron filling as well as correlation enhancement due to the ILG-induced electron doping and corresponding structural deformation.

II. RESULTS

A. Proton intercalation in Ca_2RuO_4 thin films

In this study, we used the Ca_2RuO_4 thin (∼22 nm) films, grown on $LaAlO_3$ (001) (LAO) substrates by oxide molecular beam epitaxy method (see methods in Supplemental Material [44]). Figure 1(b) shows the high-resolution x-ray diffraction (XRD) pattern of a representative thin film, confirming a single phase with good crystallinity. The films are coherently grown with the tensile strain of ∼1%, as revealed by x-ray reciprocal space mapping (RSM) (Fig. S1 [44]). The

temperature-dependent resistivity (ρ_{xx}) of the pristine thin film is shown in the upper panel of Fig. 1(c), which qualitatively agrees with previous reports [24,25]. In this curve, three characteristic temperatures T^*, T_N, and T_{MIT} [24] could be identified, based on the first derivative of ρ_{xx} [see the lower panel of Fig. 1(c)], which are 8 K, 135 K, and 195 K for the FM-like transition, AFM transition, and metal-insulator transition, respectively. Below T^*, Ca_2RuO_4 shows a drop in ρ_{xx} with non-Fermi-liquid behavior (Fig. S2 [44]). Since we do not observe any well-defined hysteresis behavior in the MR and Hall measurements until the lowest temperature, and the loop in its Hall resistivity seems weak [Figs. 3(a), S3, and S4 [44]], we refer the T^* as a transition into a canted AFM state. We note that this assignment is consistent with the previously reported "*B*-centered" magnetic mode in bulk Ca_2RuO_4 [2], exhibiting in-plane AFM ordering with FM coupling between layers.

Proton evolution and the corresponding electron doping was realized by the setup illustrated in Fig. 1(d). With the application of a positive gate voltage (V_G) between the Pt electrode and the sample, the residual water within the ionic liquid is electrolyzed, and protons were created and injected into the sample. In the process, electrons were also injected into the sample from the bottom electrode to maintain charge neutrality [29,54,55]. We first performed *in situ* x-ray diffraction (XRD) measurements of the thin film during ILG. As depicted in Fig. 1(e), for V_G smaller than 1.5 V, the Ca_2RuO_4 006 diffraction peak stays almost unchanged, while above 1.5 V this peak slowly shifts towards a lower angle and eventually saturates at 3.5 V with a relative lattice expansion of ~2.2%. The elongation of crystalline structure along out-of-plane direction through proton intercalation was also found in previous studies of oxide films [29,30,54,55]. We note that this gradual structural modification along ILG provides an equally important opportunity to manipulate the electronic and magnetic properties of Ca_2RuO_4. We also carried out *ex situ* secondary ion mass spectrometry (SIMS) measurements on ILG-samples, as shown in Fig. 1(f). Compared with a pristine sample, there is a notable increment of hydrogen concentration in the gated film, confirming the presence of proton intercalation during ILG.

B. Evolution of electronic states through proton intercalation

To explore the impact of ILG-induced proton evolution on the electronic properties of Ca_2RuO_4 films, we carried out *in situ* electrical transport (ρ_{xx}). The data, shown in Figs. 2(a) and 2(b), clearly reveal a two-step evolution around 1.5 V. This transition is also consistent with the observed characteristic voltage during the *in situ* XRD studies, where the notable structural transition occurs above 1.5 V.

In measurements below 1.5 V [Fig. 2(a)], the metallicity is gradually developed, while the metal-insulator transition temperature T_{MIT} is largely suppressed. Eventually, at about 1.45 V, the sample becomes metallic over the whole range of temperatures. The canted AFM transition, identified as a downturn in ρ_{xx} at low temperature, stays robust in the ILG measurement, as verified by peaks in $d\rho/dT$ around 8K in Fig. 2(c). On the other hand, the AFM transition, initially at 135 K, is gradually suppressed along the expanding metallic region. In addition, as guided by the gray solid line in Fig. 2(a) and blue dotted line in Fig. 2(b), the slope of the T-linear part above T_{MIT} remains nearly the same, which implies that changes in electron-phonon scattering in this range are negligible. This is consistent with the *in situ* XRD results in which little structural change can be detected for $V_G < 1.5$ V. Nonetheless, the carrier density of Ca_2RuO_4 in this region is already modified according to the Hall data measured at 100 K (see Fig. S5 [44]). Thus, we predominantly attribute this enhanced metallicity below 1.5 V to an electron-doping effect through hydrogenation. We note that the change of carrier density ($\sim 3 \times 10^{16}/cm^2$) is already substantially larger than the range (10^{14}–$10^{15}/cm^2$) of electrostatic modulation across an interface [56,57]. Therefore, we assign this change to the proton intercalation-induced charge doping. Fortunately, due to the relatively small proton concentration involved, the structural deformation is not noticeable [58]. It is interesting to note that previous study of VO_2 demonstrated that metallization can be introduced through ILG-induced bulk carrier delocalization [59], in which the intercalation of a small amount of electron can lead to a substantial structural deformation and then a dramatically enhanced conductivity. However, considering the small change of both crystal structure and electrical conductivity observed in the current system, this scenario can be safely excluded.

We next turn our focus to the second stage of evolution with $V_G \geqslant 1.5$ V [Fig. 2(b)], which shows an opposite trend with ρ_{xx} developing an upturn with decreasing temperature. The metallic region is first smeared out at low temperatures, and the sample ultimately becomes insulating. Interestingly, from the $d\rho/dT$ analysis shown in Fig. 2(c), we observe the emergence of a distinct transition at around 3–4 K, indicated by the vertical gray dotted line, which might be related to the presence of a new magnetic ground state induced by proton evolution. For the final states at moderate temperatures above this characteristic T^*, ρ_{xx} can be fitted to the two-dimensional Mott variable-range hopping model given by $\ln(\rho) \propto T^{-1/3}$, as shown in Fig. 2(e).

To sum up, the process of proton intercalation in Ca_2RuO_4 electronically drives a nonmonotonic evolution of ρ_{xx}, and the T_{MIT} at different V_G is summarized in Fig. 2(f). We note that in contrast to previous studies of ILG on perovskites of $SrRuO_3$ and $CaRuO_3$, in which the samples remain metallic through proton intercalation, the current study of Ca_2RuO_4 reveals a well-defined Mott insulating state, which highlights the important role of dimensionality for ruthenates. Moreover, the electrical conductivity of the gated film can be largely restored through thermally induced dehydrogenation (Fig. S6 [44]), which clearly suggests that the film quality is not deteriorated during the ILG.

C. Metamagnetic transition through proton intercalation

Next, we investigate the evolution of the magnetic states by measuring the evolution of magnetoresistance (MR) and anisotropic magnetoresistance (AMR) through ILG. Figure 3(a) shows the temperature-dependent in-plane MR of for pristine Ca_2RuO_4, measured with both current I and magnetic field B applied along the $[100]_o$ direction. Below T^*, it displays a pronounced positive peak around

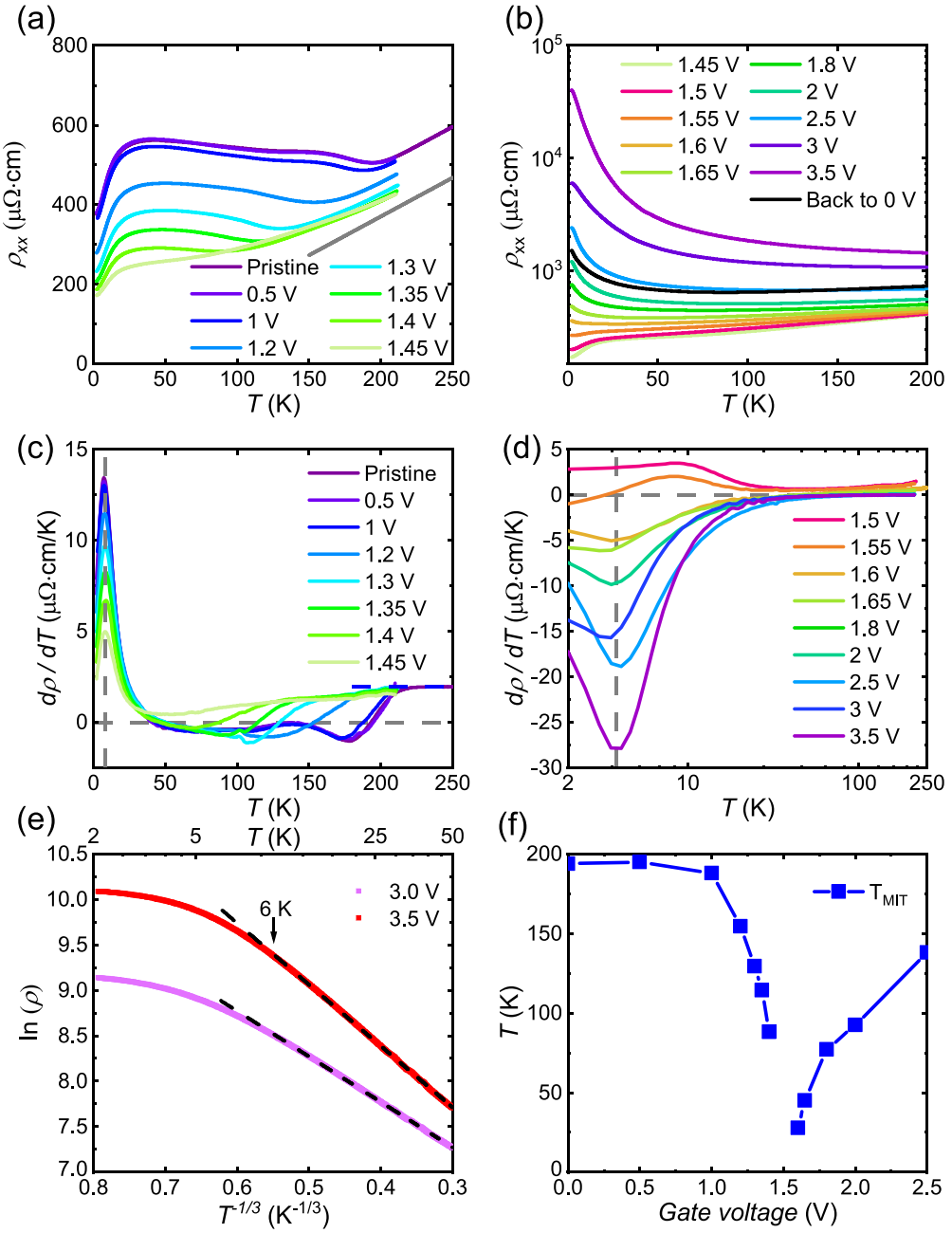

FIG. 2. *In situ* magneto-transport measurements through ILG-induced proton evolution. (a, b) Temperature dependence of resistivity ρ_{xx} at systematically increased gating voltage (V_G) below 1.5 V (a) and above 1.5 V (b). (c, d) Corresponding differentiate resistivity ($d\rho/dT$) as functions of temperature at V_G below 1.5 V (c) and above 1.5 V (d). (e) Analysis of the low-temperature resistivity in the insulating states at V_G of 3 V and 3.5 V. Black dashed lines indicate linear fits above 6 K. (f) Evolution of the metal-insulator transition temperature (T_{MIT}) at different gate voltages through ionic liquid gating.

$B = 4$ T, beyond which it decreases and becomes negative at sufficiently large field. This MR behavior coincides with the MM transition found in $Ca_{1.8}Sr_{0.2}RuO_4$, which is associated with a field destabilization of AFM coupling and leads to a state dominated by ferromagnetic-like states [11–14]. Considering the fact that compared with bulk Ca_2RuO_4, $Ca_{1.8}Sr_{0.2}RuO_4$ has slightly elongated RuO_6 octahedra with shorter in-plane lattice parameters and longer c-axis [16], the in-plane compressive strain provides similar structural modulation to Ca_2RuO_4 films, which could lead to the existence of field-induced MM transition in this system. Nevertheless, the out-of-plane MR increases positively and monotonically from 0 T to 9 T below T^* (Fig. S3 [44]), but with a tendency to saturate, indicating a larger MM transition field above 9 T along the c axis.

Similar to the electrical resistivity, the evolution of MR is also not monotonic through ILG. Below 1.5 V [Fig. 3(b)], the MM transition behavior is fairly well preserved, although the amplitude and position of its transition peak are moderately changed likely due to the electron doping. In contrast, for $V_G \geqslant 1.5$ V [Fig. 3(c)], the MR shifts downwards with an initial broadening of the MM transition peak. With further

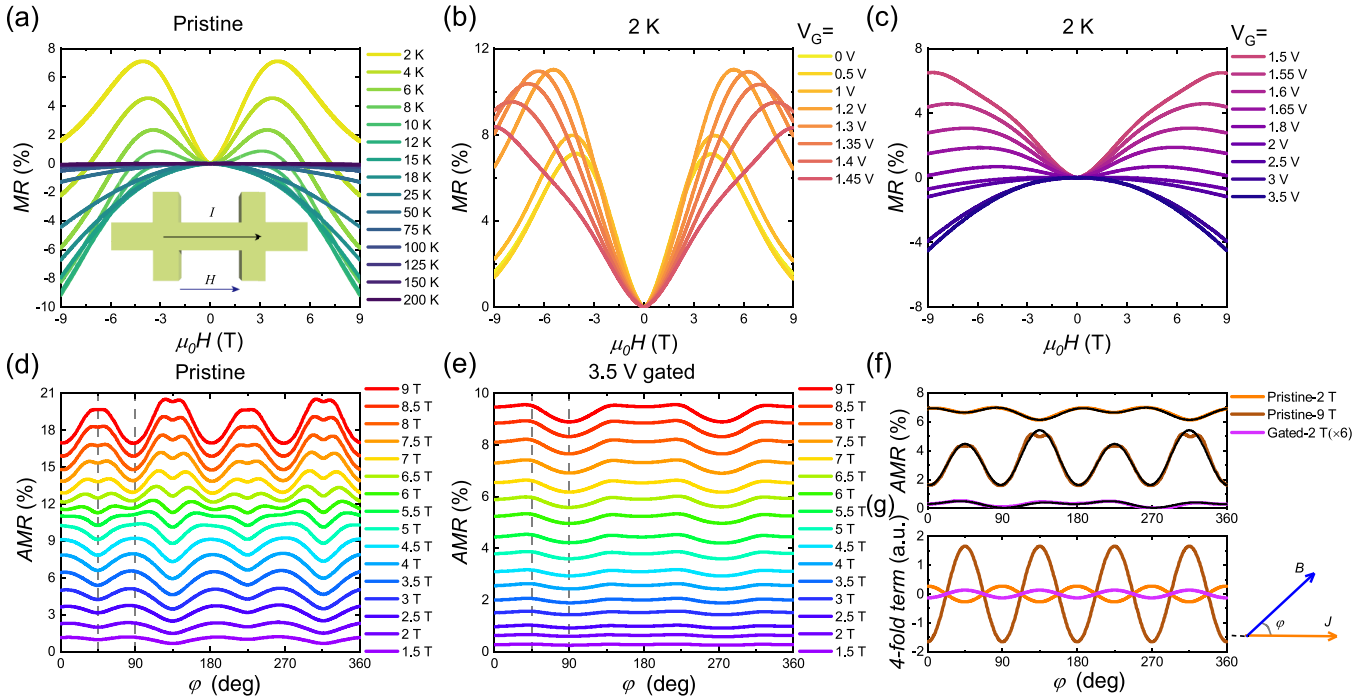

FIG. 3. Evolution of metamagnetism in Ca_2RuO_4 through ILG. (a) Magnetoresistance [MR $= \rho_{xx}(H)/\rho_{xx}(0)-1$] as a function of magnetic field for the pristine Ca_2RuO_4 thin film at various temperatures. The magnetic field was applied along the in-plane direction parallel to the current as shown in the inset. (b, c) Magnetoresistance results measured at 2 K under different V_G below 1.5 V (b) and above 1.5 V (c). (d, e) Field dependence of in-plane anisotropic magnetoresistance [AMR $= \rho_{xx}(\varphi)/\rho_{xx}(0)-1$] results as a function of angle (ϕ) between current and in-plane magnetic field [as illustrated in the inset of (g)] for pristine (d) and gated (at 3.5 V) (e) samples. Measurements were carried out at 2 K. (f) AMR measurements at 2 K of the pristine state measured at 2 T and 9 T, as well as AMR results for the gated state at 2 T (multiplied by a factor of 6). The black solid lines are the corresponding fitting curves using Eq. (1). (g) Decomposed fourfold components from the AMR fitting results for all three states shown in (f).

increase of V_G, the MR becomes completely negative and the MM transition disappears, indicating a FM interaction is gradually developed. This is a reflection of the crucial role of lattice distortion in the magnetic state of Ca_2RuO_4, recognizing that the elongation of the c axis occurs at this stage as well.

To gain a deeper understanding of the magnetic transition in this system, we measured the field-dependent in-plane AMR ($\rho_{xx}(\varphi)$) before and after ILG. Figure 3(d) shows the pristine AMR (at 2 K) as a function of ϕ between B and I under different fields. For clarity, all curves are shifted vertically. At low field, the results can be decomposed into a superposition of data with twofold and fourfold periodicity. It is noteworthy that a similar AMR effect with a mixture of twofold and fourfold symmetric components was reported in other canted AFM systems especially layered Sr_2IrO_4 and (Sr, Ca)IrO_3/$SrTiO_3$ heterostructures [60–63]. For these materials, the twofold symmetry in AMR was proposed to be a signature of magneto-elastic coupling, which gives rise to an orthorhombic distortion under external magnetic field leading to the enhanced uniaxial anisotropy [60,64]. The fourfold signal in AMR is suggested to be associated with the intrinsic biaxial magnetocrystalline anisotropy [60,63] imposed by the pseudocubic LAO substrate. From Fig. 3(d), with increasing magnetic field, the AMR undergoes a transition to a state with dominant fourfold symmetry at $B = 9$ T. These curves are also illustrated by polar plots in Fig. S7 [44] for clarity. Additionally, the positions of peaks in the AMR curves measured at low fields are shifted by approximately 45° for high-field measurements. For example, as indicated by gray dotted lines in Fig. 3(d), the local maximum of AMR at about $\varphi = 0°$ under $B = 1.5$ T, moves to near $\varphi = 45°$ for $B = 9$ T; and likewise, the local minimum at $\varphi = 45°$ evolves to $\varphi = 90°$. Consistent with our MR measurements for the pristine state, the transformation of the AMR above $B = 4$ T also suggests the occurrence of a MM transition.

In comparison, the AMR measured at 2 K for the sample gated at 3.5 V shows no sign of a magnetic transition [Fig. 3(e) and Fig. S8 [44]], which is also in agreement with the MR results for Ca_2RuO_4 under large gate voltages. We point out that the peaks and minima in Fig. 3(e) show up at similar angles as in the AMR of pristine Ca_2RuO_4 at $B = 9$ T. This observation implies the similarity in magnetic states between Ca_2RuO_4 at high fields above MM transition and Ca_2RuO_4 after proton intercalation. More importantly, the AMR of gated (at 3.5 V) Ca_2RuO_4 in Fig. 3(e) shows great similarity to the previously reported AMR of $Ca_{1.8}Sr_{0.2}RuO_4$ at high fields across the metamagnetic transition [13].

To clarify the detailed AMR transition under external field and ILG, we adopted an empirical expression to analyze the

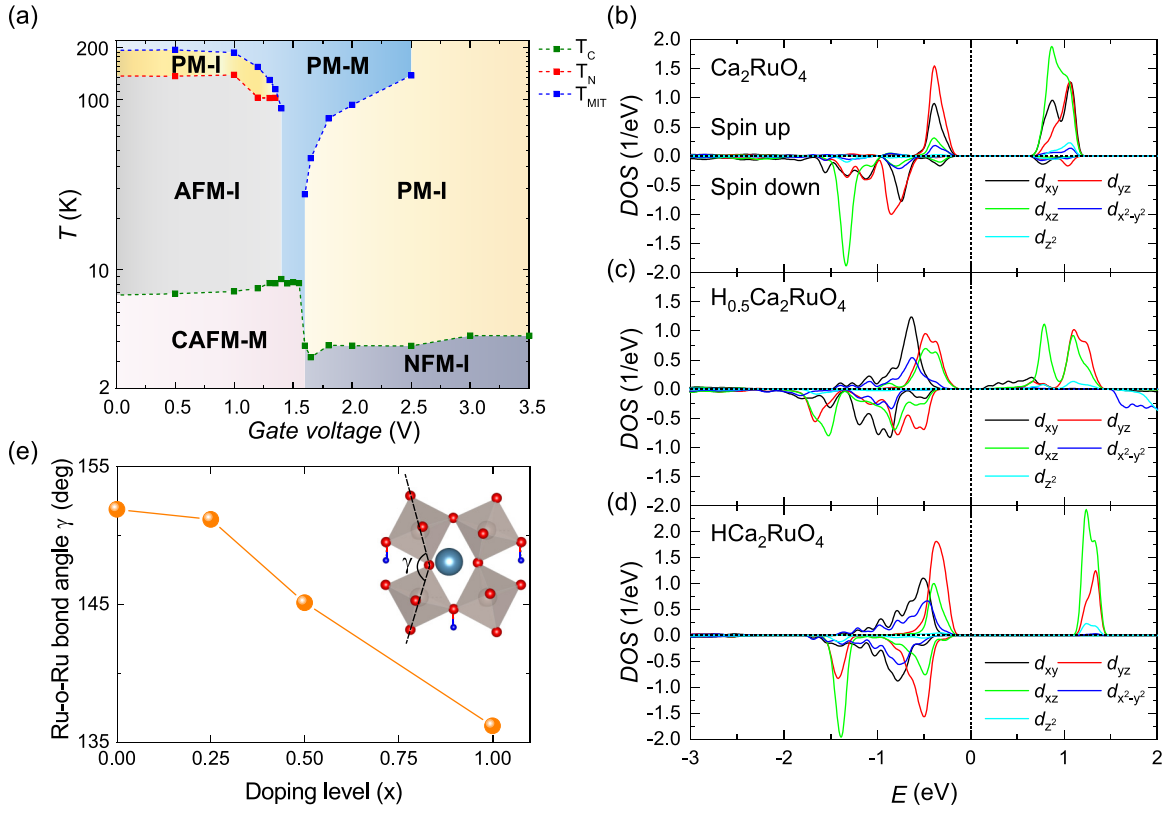

FIG. 4. Evolution of electronic and magnetic states of Ca_2RuO_4 through ILG-induced structural modification and electron doping. (a) Schematic phase diagram of the Ca_2RuO_4 with ILG. The pristine state is a canted AFM metal (CAFM-M) below 8 K, while with increasing temperature it goes through a series of intermediate states including an AFM insulating (AFM-I) state and a paramagnetic insulating (PM-I) state, and then finally becomes a paramagnetic metal (PM-M) at ∼200 K. At a mild gating voltage slightly lower than 1.5 V, the intermediate insulating region is suppressed to achieve a pronounced paramagnetic metallic state. As V_G continues to increase above 1.5 V, the ground state of Ca_2RuO_4 evolves into a near FM insulator (NFM-I) at lower temperature, and a paramagnetic insulator (PM-I) at higher temperatures. (b–d) Spin-polarized density of states (DOS) of Ca_2RuO_4 (b), $H_{0.5}Ca_2RuO_4$ (c), and HCa_2RuO_4 (d) obtained through DFT + U calculations. The vertical dashed line denotes the position of the Fermi level, which is taken to be the origin of the horizontal axis. (e) Calculated Ru-O-Ru bond angles at different proton doping levels (x) of $H_xCa_2RuO_4$. The inset figure shows an illustration of the octahedral rotation of the $H_{0.5}Ca_2RuO_4$ layer viewed from the c-axis direction.

measured angular-dependent resistivity $\rho_{xx}(\varphi)$ as,

$$\rho_{xx}(\varphi) = C_0 + C_2\cos[2(\varphi+\psi_2)] + C_4\cos[4(\varphi+\psi_4)], \quad (1)$$

where C_0, C_2, and C_4 are fitting constants, and $\cos[2(\varphi+\psi_2)]$ and $\cos[4(\varphi+\psi_4)]$ account for contributions from twofold and fourfold components, respectively. In Fig. 3(f) we display the fits of AMR data for three representative states that correspond to pristine states at low field ($B = 2$ T) and high field ($B = 9$ T), as well as the gated state at low field ($B = 2$ T). All three curves are well described using Eq. (1) in Fig. 3(f). Considering previous studies of $Ca_{1.8}Sr_{0.2}RuO_4$, which revealed that the emergence of the MM transition is essentially connected with the fourfold periodicity in AMR [13], we extract the fourfold contribution from AMR of all these states. As plotted in Fig. 3(g), a comparison between pristine AMR at $B = 2$ T and $B = 9$ T clearly shows that the MM transition in Ca_2RuO_4 leads to a phase shift of 45° in its fourfold component. Interestingly, the AMR of the gated state at $B = 2$ T has the same amount of phase shift as that of the pristine state at $B = 9$ T. This result clearly suggests that proton intercalation induces a MM transition in Ca_2RuO_4 films, and the magnetic state after the MM transition is close to FM [11–14], in accordance with the negative MR observed in Fig. 3(c). We want to remark that in contrast to the conventional field-induced MM transitions, the MM transition observed in the current study is driven by the ILG-induced electron doping.

D. Discussion

With the picture of electronic and magnetic evolution with ILG, we are able to construct a phase diagram to summarize the properties of Ca_2RuO_4 as a function of gate voltage and temperature, as shown in Fig. 4(a). The initial state is metallic with canted AFM order at low temperature, followed by an insulating region dominated by AFM order, and then a metallic state at higher temperatures. The intermediate insulating region is gradually narrowed with ILG, and eventually a completely metallic state is developed around 1.5 V. Specifically, the electron doping through ILG gradually turns the insulating state of our sample into a metallic state, leading to the suppression of T_{MIT}, as reflected in Fig. 4(a). We tend to attribute this change to an intrinsic change of electronic state of Ca_2RuO_4 through electron doping. However, we note that in the vicinity

of the metal-insulator transition, there often exists a mixed phase of metallic and insulating phases [18], and thus it might also be possible that the ILG induces a mixture of metallic and insulating Ca_2RuO_4 along this phase transition. Nevertheless, the essential feature of these two scenarios is the emergent metallic state through hydrogenation-induced doping, which will be further elaborated through theoretical calculations as shown below, while, further increase of V_G triggers significant structural modifications of Ca_2RuO_4 [Fig. 1(e)], and the sample becomes insulating for the whole temperature range studied, and a near FM state is developed below ~4 K, resulting from a MM transition triggered by ILG-induced electron doping.

To further unveil the underlying mechanism of the electronic and magnetic transitions in Ca_2RuO_4 through ILG, we performed density-functional theory calculations with Coulomb corrections (DFT+U) to investigate the effects of proton intercalation on the 4d orbitals of Ru ions. The details are presented in the Supplemental Material [44]. The optimized crystalline structures of $H_xCa_2RuO_4$ ($x = 0.25,\ 0.5,\ 1$) are shown in Fig. S9 [44], in which at lower hydrogen concentrations the introduced protons tend to form O-H bonds with the apical oxygen ions of the RuO_6 octahedra ($x = 0.25$) at the CaO layer, while at higher concentrations they are bonded with the equatorial oxygen at the RuO_2 layers.

Figures 4(b)–4(d) present the calculated spin-polarized band structures for the pristine Ca_2RuO_4, moderately protonated $H_{0.5}Ca_2RuO_4$ and highly protonated HCa_2RuO_4 samples, respectively. The pristine Ca_2RuO_4 is shown to prefer an in-plane G-type antiferromagnetic order (Table. S1 [44]), consistent with our experimental observations of significant positive MR [Fig. 2(a)] and weak magnetization (Fig. S10 [44]) at 2 K. While this G-type AFM causes the existence of a sizable band gap (Fig. 4(b)), we attribute the drop in ρ_{xx} below T^* of the pristine Ca_2RuO_4 [Fig. 1(c)] to the canted AFM-induced enhancement of conductivity, which is similar to that found in Sr_2IrO_4 [61]. Our theoretical calculations reveal that with the in-plane lattice parameters fixed by the compressive strain from LAO substrate, the intercalation of protons into the RuO_2 layers leads to a decrease of the Ru-O-Ru bond angle as depicted in Fig. 4(e), indicating an enlarged rotational distortion of the RuO_6 octahedra. Consequently, the hybridization between the equatorial oxygen and the d_{xy} states is weakened, which results in a downward shift of d_{xy} band [65]. Combined with the proton evolution-induced electron doping effect, the system is expected to be more conductive. This is manifested in Fig. 4(c) that the unoccupied d_{xy} orbital moves toward the Fermi level, and the band gap of $H_{0.5}Ca_2RuO_4$ is remarkably reduced. With further increasing V_G, the Ru ions would be dramatically doped with electrons as demonstrated in the perovskite $SrRuO_3$ and $CaRuO_3$ [29,30], approaching a band configuration with five electrons occupying t_{2g} orbitals. Additionally, the in-plane Ru-O-Ru bond angle continues to decrease to 136° in HCa_2RuO_4 [Fig. 4(e)]. As a result, the hybridization among 4d orbitals of Ru is strengthened, and the electron correlation effect is tremendously enhanced, which leads to a narrower bandwidth and the emergence of a larger band gap in the electronic configuration of HCa_2RuO_4 as shown in Fig. 4(d), indicating the tendency towards a Mott insulating state. This evolution of electronic band structure along the proton evolution is qualitatively consistent with the nonmonotonic evolution of ρ_{xx} we observed in the ILG experiment. The significant modulation of the band dispersion of Ca_2RuO_4 can also be clearly seen in the calculated non-spin-polarized band structures for the pristine and protonated samples (see Fig. S11 [44]). Besides, the larger distortion weakens the super-exchange interaction mediated by the oxygen ions and enhances the direct-exchange interaction between Ru ions. Accordingly, the in-plane ferromagnetic coupling becomes dominant in the HCa_2RuO_4 phase, and consequently both FM and A-type AFM orders become more energetically stable compared to the G-type AFM order in pristine Ca_2RuO_4 (Table. S1 [44]), which explains the observed near FM state under high gate voltage. The relatively low transition temperature should be attributed to the strong magnetic instability caused by the competition between FM and AFM interactions.

It is worth noting that the insulating state of HCa_2RuO_4 with strong electron correlation is distinct from the results of the previous studies of this material. Both the strontium-doped bulk system $Ca_{2-x}Sr_xRuO_4$ [15–19] and pressurized pure single crystals [20–22] reveal a metallic state through structural modification in which the c axis is elongated. Meanwhile, researchers also demonstrated that the substitution of Ca with La or Pr can also lead to a metallic state with slight electron doping [26–28]. In this work, with the application of the ILG-induced proton evolution, we significantly extend the phase diagram upon electron doping in this interesting oxide system, and achieve an exotic insulating state with five electrons on the 4d orbitals and a moment $S = 1/2$ per Ru ion (Table S2 [44]). It is interesting to note that HCa_2RuO_4 shows great similarities in terms of structure and magnetic configuration with Sr_2IrO_4, a layered Mott insulator with $J_{\text{eff}} = 1/2$ state [66]. While different from Sr_2IrO_4, in which the band gap is introduced through the combination of spin-orbit coupling and Coulomb interaction, the band gap in HCa_2RuO_4 is caused predominately by the strong electron correlation due to the structural deformation. Since many intriguing correlated phenomena including Fermi arcs, pseudogaps, and nontrivial broken symmetry phases have been observed in the electron-doped and hole-doped Sr_2IrO_4 in proximity to its Mott state [67–70], we believe that the realization of HCa_2RuO_4 with $S = 1/2$ provides an interesting platform to explore the extraordinary hidden phases in the quasi-two-dimensional layered perovskites. Furthermore, our Hall measurements reveal a sign change of Hall resistivity (at 2 K) when V_G exceeds 1.5 V (Fig. S12 [44]), which can be attributed to the change of Berry curvature with electron doping. Knowing that the electric field-induced Mott transition provides a pave way for the next-generation nonvolatile memory [71], the realization of the exotic insulating state of HCa_2RuO_4 through proton intercalation in this work may also inspire more high-performance Mott memory devices.

III. CONCLUSION

In summary, we present an experimental and theoretical study of the evolution of electronic and magnetic states of Ca_2RuO_4 thin films through the ILG-induced proton

intercalation. We attribute the ground state evolution to the manipulation of both the charge and lattice degrees of freedom, in which the electron doping first enhances the metallicity of Ca_2RuO_4 at lower doping level, then with subsequent structural deformation, the system is driven into an insulating state in proximity to ferromagnetism. Our work not only helps us to understand the complex magnetic transitions in Ca_2RuO_4 and enriches the phase diagram of ruthenates, but also displays a promising opportunity to manipulate the electronic and magnetic properties of correlated quantum materials.

ACKNOWLEDGMENTS

This study was financially supported by the National Basic Research Program of China (No. 2021YFE0107900); the National Natural Science Foundation of China (No. 52025024); the Basic Science Center Program of NSFC (No. 52388201); and the Beijing Nature Science Foundation (No. Z200007). This research was funded in part by the Gordon and Betty Moore Foundation's EPiQS Initiative through Grants No. GBMF3850 and No. GBMF9073 to Cornell University. Sample preparation was, in part, facilitated by the Cornell NanoScale Facility, a member of the National Nanotechnology Coordinated Infrastructure (NNCI), which is supported by the National Science Foundation (Grant No. NNCI-2025233). Research at Cornell was supported by the Air Force Office of Scientific Research (Grant No. FA9550-21-1–0168) and the National Science Foundation (No. DMR-2104427). L.S. thanks the starting funds from Northwest University and funding through the Austrian Science Fund (FWF) project I 5398. Calculations have been mainly done on the Vienna Scientific Cluster (VSC).

[1] Y. Maeno, Superconductivity in a layered perovskite without copper, Nature (London) **372**, 532 (1994).

[2] M. Braden, G. André, S. Nakatsuji, and Y. Maeno, Crystal and magnetic structure of Ca_2RuO_4: Magnetoelastic coupling and the metal-insulator transition, Phys. Rev. B **58**, 847 (1998).

[3] A. V. Puchkov, M. C. Schabel, D. N. Basov, T. Startseva, G. Cao, T. Timusk, and Z. X. Shen, Layered ruthenium oxides: From band metal to Mott insulator, Phys. Rev. Lett. **81**, 2747 (1998).

[4] J. H. Jung, Z. Fang, J. P. He, Y. Kaneko, Y. Okimoto, and Y. Tokura, Change of electronic structure in Ca_2RuO_4 induced by orbital ordering, Phys. Rev. Lett. **91**, 056403 (2003).

[5] I. Zegkinoglou, Orbital ordering transition in Ca_2RuO_4 observed with resonant x-ray diffraction, Phys. Rev. Lett. **95**, 136401 (2005).

[6] A. Jain, Higgs mode and its decay in a two-dimensional antiferromagnet, Nat. Phys. **13**, 633 (2017).

[7] S. M. Souliou, J. Chaloupka, G. Khaliullin, G. Ryu, A. Jain, B. J. Kim, M. L. Tacon, and B. Keimer, Raman scattering from higgs mode oscillations in the two-dimensional antiferromagnet Ca_2RuO_4, Phys. Rev. Lett. **119**, 067201 (2017).

[8] C. S. Alexander, G. Cao, V. Dobrosavlijevic, S. McCall, and J. E. Crow, E. Lochner, and R. P. Guertin, Destruction of the Mott insulating ground state of Ca_2RuO_4 by a structural transition, Phys. Rev. B **60**, R8422 (1999).

[9] X. Li, H. Ning, O. Mehio, H. Zhao, M. C. Lee, K. Kim, F. Nakamura, Y. Maeno, G. Cao, and D. Hsieh, Keldysh space control of charge dynamics in a strongly driven Mott insulator, Phys. Rev. Lett. **128**, 187402 (2022).

[10] K. Uchida, G. Mattoni, S. Yonezawa, F. Nakamura, Y. Maeno, and K. Tanaka, High-order harmonic generation and its unconventional scaling law in the Mott-insulating Ca_2RuO_4, Phys. Rev. Lett. **128**, 127401 (2022).

[11] S. Nakatsuji, D. Hall, L. Balicas, Z. Fisk, K. Sugahara, M. Yoshioka, and Y. Maeno, Heavy-mass Fermi liquid near a ferromagnetic instability in layered ruthenates, Phys. Rev. Lett. **90**, 137202 (2003).

[12] L. Balicas, S. Nakatsuji, D. Hall, Z. Fisk, and Y. Maeno, Metamagnetism in $Ca_{2-x}Sr_xRuO_4$ in the verge of the Mott transition, Physica B **346–347**, 344 (2004).

[13] L. Balicas, S. Nakatsuji, D. Hall, T. Ohnishi, Z. Fisk, Y. Maeno, and D. J. Singh, Severe Fermi surface reconstruction at a metamagnetic transition in $Ca_{2-x}Sr_xRuO_4$ (for $0.2 \leqslant x \leqslant 0.5$), Phys. Rev. Lett. **95**, 196407 (2005).

[14] M. Kriener, Structural aspects of metamagnetism in $Ca_{2-x}Sr_xRuO_4$: Evidence for field tuning of orbital occupation, Phys. Rev. Lett. **95**, 267403 (2005).

[15] S. Nakatsuji and Y. Maeno, Quasi-two-dimensional Mott transition system $Ca_{2-x}Sr_xRuO_4$, Phys. Rev. Lett. **84**, 2666 (2000).

[16] S. Nakatsuji and Y. Maeno, Switching of magnetic coupling by a structural symmetry change near the Mott transition in $Ca_{2-x}Sr_xRuO_4$, Phys. Rev. B **62**, 6458 (2000).

[17] G. Cao, C. S. Alexander, S. McCall, J. E. Crow, and R. P. Guertin, Ferromagnetic polarons in dilute La-doped Ca_2RuO_4, J. Magn. Magn. Mater. **226–230**, 235 (2001).

[18] O. Friedt, M. Braden, G. Andre, P. Adelmann, S. Nakatsuji, and Y. Maeno, Structural and magnetic aspects of the metal-insulator transition in $Ca_{2-x}Sr_xRuO_4$, Phys. Rev. B **63**, 174432 (2001).

[19] J. P. Carlo, New magnetic phase diagram of $(Sr, Ca)_2RuO_4$, Nat. Mater. **11**, 323 (2012).

[20] F. Nakamura, T. Goko, M. Ito, T. Fujita, S. Nakatsuji, H. Fukazawa, Y. Maeno, P. Alireza, D. Forsythe, and S. R. Julian, From Mott insulator to ferromagnetic metal: A pressure study of Ca_2RuO_4, Phys. Rev. B **65**, 220402(R) (2002).

[21] P. Steffens, High-pressure diffraction studies on Ca_2RuO_4, Phys. Rev. B **72**, 094104 (2005).

[22] F. Nakamura, R. Nakai, T. Takemoto, M. Sakaki, T. Suzuki, P. L. Alireza, S. Nakatsuji, and Y. Maeno, Anisotropic giant magnetoresistance near the Mott transition in pressurized Ca_2RuO_4, Phys. Rev. B **80**, 193103 (2009).

[23] X. Wang, Y. Xin, P. A. Stampe, R. J. Kennedy, and J. P. Zheng, Epitaxial thin film growth of $Ca_2RuO_{4+\delta}$ by pulsed laser deposition, Appl. Phys. Lett. **85**, 6146 (2004).

[24] L. Miao, P. Silwal, X. Zhou, I. Stern, J. Peng, W. Zhang, L. Spinu, Z. Mao, and D. H. Kim, Itinerant ferromagnetism and geometrically suppressed metal-insulator transition in epitaxial thin films of Ca_2RuO_4, Appl. Phys. Lett. **100**, 052401 (2012).

[25] C. Dietl, Tailoring the electronic properties of Ca_2RuO_4 via epitaxial strain, Appl. Phys. Lett. **112**, 031902 (2018).

[26] H. Fukazawa and Y. Maeno, Filling control of the Mott insulator Ca_2RuO_4, J. Phys. Soc. Jpn. **70**, 460 (2001).

[27] D. Pincini, Persistence of antiferromagnetic order upon La substitution in the $4d^4$ Mott insulator Ca_2RuO_4, Phys. Rev. B **98**, 014429 (2018); D. Pincini, L. S. I. Veiga, C. D. Dashwood, F. Forte, M. Cuoco, R. S. Perry, P. Bencok, A. T. Boothroyd, and D. F. McMorrow, Tuning of the Ru^{4+} ground-state orbital population in the $4d^4$ Mott insulator Ca_2RuO_4 achieved by La doping, *ibid.* **99**, 075125 (2019).

[28] S. Ricco, In situ strain tuning of the metal-insulator-transition of Ca_2RuO_4 in angle-resolved photoemission experiments, Nat. Commun. **9**, 4535 (2018).

[29] Z. Li, Reversible manipulation of the magnetic state in $SrRuO_3$ through electric-field controlled proton evolution, Nat. Commun. **11**, 184 (2020).

[30] S. Shen, Z. Li, Z. Tian, W. Luo, S. Okamoto, and P. Yu, Emergent ferromagnetism with Fermi-liquid behavior in proton intercalated $CaRuO_3$, Phys. Rev. X **11**, 021018 (2021).

[31] W. Lin, Electric field control of the magnetic Weyl fermion in an epitaxial $SrRuO_3$ (111) thin film, Adv. Mater. **33**, e2101316 (2021).

[32] H. Han, Reversal of anomalous Hall effect and octahedral tilting in $SrRuO_3$ thin films via hydrogen spillover, Adv. Mater. **35**, 2207246 (2023).

[33] V. I. Anisimov, I. A. Nekrasov, D. E. Kondakov, T. M. Rice, and M. Sigrist, Orbital-selective Mott-insulator transition in $Ca_{2-x}Sr_xRuO_4$, Eur. Phys. J. B **25**, 191 (2002).

[34] A. Koga, N. Kawakami, T. M. Rice, and M. Sigrist, Orbital-selective Mott transitions in the degenerate Hubbard model, Phys. Rev. Lett. **92**, 216402 (2004).

[35] S. C. Wang, Fermi surface topology of $Ca_{1.5}Sr_{0.5}RuO_4$ determined by angle-resolved photoelectron spectroscopy, Phys. Rev. Lett. **93**, 177007 (2004).

[36] J. S. Lee, S. J. Moon, T. W. Noh, S. Nakatsuji, and Y. Maeno, Orbital-selective mass enhancements in multiband $Ca_{2-x}Sr_xRuO_4$ systems analyzed by the extended Drude model, Phys. Rev. Lett. **96**, 057401 (2006).

[37] E. Ko, B. J. Kim, C. Kim, and H. J. Choi, Strong orbital-dependent d-band hybridization and Fermi-surface reconstruction in metallic $Ca_{2-x}Sr_xRuO_4$, Phys. Rev. Lett. **98**, 226401 (2007).

[38] A. Liebsch and H. Ishida, Subband filling and Mott transition in $Ca_{2-x}Sr_xRuO_4$, Phys. Rev. Lett. **98**, 216403 (2007).

[39] M. Neupane, Observation of a novel orbital selective Mott transition in $Ca_{1.8}Sr_{0.2}RuO_4$, Phys. Rev. Lett. **103**, 097001 (2009).

[40] A. Shimoyamada, K. Ishizaka, S. Tsuda, S. Nakatsuji, Y. Maeno, and S. Shin, Strong mass renormalization at a local momentum space in multiorbital $Ca_{1.8}Sr_{0.2}RuO_4$, Phys. Rev. Lett. **102**, 086401 (2009).

[41] E. Gorelov, M. Karolak, T. O. Wehling, F. Lechermann, A. I. Lichtenstein, and E. Pavarini, Nature of the mott transition in Ca_2RuO_4, Phys. Rev. Lett. **104**, 226401 (2010).

[42] D. Sutter, Orbitally selective breakdown of Fermi liquid quasiparticles in $Ca_{1.8}Sr_{0.2}RuO_4$, Phys. Rev. B **99**, 121115(R) (2019).

[43] M. Kim, Signature of Kondo hybridisation with an orbital-selective Mott phase in 4D $Ca_{2-x}Sr_xRuO_4$, npj Quantum Mater. **7**, 59 (2022).

[44] See Supplemental Material at http://link.aps.org/supplemental/10.1103/PhysRevMaterials.8.074408 for methods and supplemental figures. It also contains Refs. [45–53].

[45] H. P. Nair, Demystifying the growth of superconducting Sr_2RuO_4 thin films, APL Mater. **6**, 101108 (2018).

[46] P. Hohenberg and W. Kohn, Inhomogeneous electron gas, Phys. Rev. **136**, B864 (1964).

[47] W. Kohn and L. J. Sham, Self-consistent equations including exchange and correlation effects, Phys. Rev. **140**, A1133 (1965).

[48] V. I. Anisimov, J. Zaanen, and O. K. Andersen, Band theory and Mott insulators: Hubbard U instead of Stoner I, Phys. Rev. B **44**, 943 (1991).

[49] G. Kresse and J. Furthmüller, Efficient iterative schemes for *ab initio* total-energy calculations using a plane-wave basis set, Phys. Rev. B **54**, 11169 (1996).

[50] G. Kresse and J. Furthmüller, Efficiency of ab-initio total energy calculations for metals and semiconductors using a plane-wave basis set, Comput. Mater. Sci. **6**, 15 (1996).

[51] J. P. Perdew, K. Burke, and M. Ernzerhof, Generalized gradient approximation made simple, Phys. Rev. Lett. **77**, 3865 (1996).

[52] S. L. Dudarev, G. A. Botton, S. Y. Savrasov, C. J. Humphreys, and A. P. Sutton, Electron-energy-loss spectra and the structural stability of nickel oxide: An LSDA+ U study, Phys. Rev. B **57**, 1505 (1998).

[53] L. Si, O. Janson, G. Li, Z. Zhong, Z. Liao, G. Koster, and K. Held, Quantum anomalous hall state in ferromagnetic $SrRuO_3$ (111) bilayers, Phys. Rev. Lett. **119**, 026402 (2017).

[54] N. Lu, Electric-field control of tri-state phase transformation with a selective dual-ion switch, Nature (London) **546**, 124 (2017).

[55] M. Wang, Electric-Field-Controlled phase transformation in WO_3 thin films through hydrogen evolution, Adv. Mater. **29**, 1703628 (2017).

[56] C. H. Ahn, J. M. Triscone, and J. Mannhart, Electric field effect in correlated oxide systems, Nature (London) **424**, 1015 (2003).

[57] C. H. Ahn, Electrostatic modification of novel materials, Rev. Mod. Phys. **78**, 1185 (2006).

[58] M. Wang, Manipulation of the electronic state of mott iridate superlattice through protonation induced electron-filling, Adv. Funct. Mater. **31**, 2100261 (2021).

[59] M. Nakano, K. Shibuya, D. Okuyama, T. Hatano, S. Ono, M. Kawasaki, Y. Iwasa, and Y. Tokura, Collective bulk carrier delocalization driven by electrostatic surface charge accumulation, Nature (London) **487**, 459 (2012).

[60] C. Wang, H. Seinige, G. Cao, J. S. Zhou, J. B. Goodenough, and M. Tsoi, Anisotropic magnetoresistance in antiferromagnetic Sr_2IrO_4, Phys. Rev. X **4**, 041034 (2014).

[61] H. Wang, Giant anisotropic magnetoresistance and nonvolatile memory in canted antiferromagnet Sr_2IrO_4, Nat. Commun. **10**, 2280 (2019).

[62] Z. S. Lim, Magnetic anisotropy of a quasi two-dimensional canted antiferromagnet, Nano Lett. **20**, 1890 (2020).

[63] M. Vagadia, Extraordinary anisotropic magnetoresistance in $CaMnO_3/CaIrO_3$ heterostructures, Phys. Rev. B **105**, L020402 (2022).

[64] H. Liu and G. Khaliullin, Pseudo-Jahn-Teller effect and magnetoelastic coupling in spin-orbit Mott insulators, Phys. Rev. Lett. **122**, 057203 (2019).

[65] Z. Fang, and K. Terakura, Magnetic phase diagram of Ca_2RuO_4 governed by structural distortions, Phys. Rev. B **64**, 020509(R) (2001); Z. Fang, N. Nagaosa, and K. Terakura, Orbital-dependent phase control in $Ca_{2-x}Sr_xRuO_4$ ($0 \leqslant x \leqslant 0.5$), *ibid.* **69**, 045116 (2004).

[66] B. J. Kim, Novel $J_{\text{eff}} = 1/2$ Mott state induced by relativistic spin-orbit coupling in Sr_2IrO_4, Phys. Rev. Lett. **101**, 076402 (2008).

[67] Y. K. Kim, O. Krupin, J. D. Denlinger, A. Bostwick, E. Rotenberg, Q. Zhao, J. F. Mitchell, J. W. Allen, and B. J. Kim, Fermi arcs in a doped pseudospin-1/2 Heisenberg antiferromagnet, Science **345**, 187 (2014).

[68] Y. K. Kim, N. H. Sung, J. D. Denlinger, and B. J. Kim, Observation of a d-wave gap in electron-doped Sr_2IrO_4, Nat. Phys. **12**, 37 (2015).

[69] L. Zhao, D. H. Torchinsky, H. Chu, V. Ivanov, R. Lifshitz, R. Flint, T. Qi, G. Cao, and D. Hsieh, Evidence of an odd-parity hidden order in a spin–orbit coupled correlated iridate, Nat. Phys. **12**, 32 (2015).

[70] C. Lu. and J. M. Liu, The $J_{\text{eff}} = 1/2$ antiferromagnet Sr_2IrO_4: A golden avenue toward new physics and functions, Adv. Mater. **32**, 1904508 (2020).

[71] Y. Zhou and S. Ramanathan, Mott memory and neuromorphic devices, Proc. IEEE **103**, 1289 (2015).

Supplementary Materials of

"Tuning the electronic and magnetic states of Ca_2RuO_4 with proton evolution"

Di Tian[1#], Ludi Miao[2,3#], Liang Si[4,5#], Nathaniel J. Schreiber[6], Shengchun Shen[1], Jianbing Zhang[1], Xinyu Shu[1], Xiaochao Wang[4], Hari P. Nair[6], Jacob P. Ruf[2], Darrell G. Schlom[6,7,8*], Kyle M. Shen[2,7*] and Pu Yu[1,9*]

[1] *State Key Laboratory of Low Dimensional Quantum Physics and Department of Physics, Tsinghua University, 100084 Beijing, China*
[2] *Department of Physics, Laboratory of Atomic and Solid State Physics, Cornell University, Ithaca, New York 14853, USA*
[3] *Department of Physics, New Mexico State University, Las Cruces, NM 88003, USA*
[4] *School of Physics, Northwest University, Xi'an 710127, China*
[5] *Institut für Festkörperphysik, TU Wien, 1040 Vienna, Austria*
[6] *Department of Materials Science and Engineering, Cornell University, Ithaca, New York 14853, USA*
[7] *Kavli Institute at Cornell for Nanoscale Science, Ithaca, New York 14853, USA*
[8] *Leibniz-Institut für Kristallzüchtung, Max-Born-Str. 2, 12489 Berlin, Germany*
[9] *Frontier Science Center for Quantum Information, 100084 Beijing, China*

#These authors contributed to this work equally.

**Correspondence should be addressed to:* schlom@cornell.edu, kmshen@cornell.edu *and* yupu@tsinghua.edu.cn

Methods

Growth of Ca_2RuO_4 films. All samples were prepared by reactive oxide molecular-beam epitaxy in an absorption-controlled regime [1], which reduces the defects related to cation non-stoichiometry, especially ruthenium vacancies. The Ca_2RuO_4 films were grown at a substrate temperature of 1000 ^oC, and a background oxidant partial pressure of 10^{-6} Torr of distilled ozone (80% O_3 + 20% O_2).

***In-situ* XRD measurements. X-ray diffraction (**XRD) and X-ray reciprocal space mapping (RSM) measurements were performed with a high-resolution diffractometer (Smartlab, Rigaku) using monochromatic Cu Kα1 radiation (λ = 1.5406 Å) at room temperature. For *in-situ* measurements, we used a rectangular Pt flake as the gated electrode, and the thin film sample as the ground. Then both the sample and Pt were placed in a quartz bowl on the sample-holder of the XRD diffractometer. A small amount of ionic liquid was added into the bowl to cover the entire sample, while its amount was carefully controlled to obtain reasonable high X-ray transmission.

***In-situ* electrical transport measurements.** The transport measurements were performed in a PPMS setup (Quantum Design DynaCool system, 9 T) equipped with lock-in amplifiers (Model LI 5640, NF Corporation). Hall bar devices (220 μm × 60 μm) were fabricated through standard lithography/etching method from the thin-film samples and the electrodes were capped with sputtered Ti/Au. Then the sample was placed in a quartz bowl covered entirely with ionic liquid (DEME-TFSI), and a slice of Pt was used as the gate electrode. For each gating state, the gating voltage (V_G) was gradually changed to the desired voltage, and then held for 15 minutes at 295 K to achieve a fully reacted state. Finally, the sample was cooled down below 230 K to freeze the ionic liquid, below which the electrochemical reaction was stopped, and then the detailed magnetotransport studies were systematically carried out.

SIMS measurements. Secondary ion mass spectrometry (SIMS) measurements were carried out using a TOF.SIMS 5-100 instrument (IONTOF GmbH) to probe the hydrogen concentration of the gated samples. The sputtering area was 250 μm × 250 μm and the detecting

area was set as 100 μm × 100 μm to minimize the influence of the edge region. The interface position between thin film and substrate was indexed through measurements of Al and La elements from the $LaAlO_3$ substrate, and the H concentration was simultaneously measured. All samples were measured under the same conditions.

First-principles calculations: Density-functional theory plus coulomb *U* (DFT+*U*) [2-4] calculations were performed to investigate the structural, electronic and magnetic properties of Ca_2RuO_4 and $H_xCa_2RuO_4$, using Vienna Ab-initio Simulation Package (Vasp) [5,6] and Perdew-Burke-Ernzerh of exchange-correlation functional within the generalized gradient approximation (GGA-PBE) [7]. The valence states considered include the 3s3p4s, 4p5s4d, 2s2p and 1s states of Ca, Ru, O and H atom. Electronic wave-functions were expanded using a plane-wave basis set [5,6] with a kinetic energy cut-off of 600eV that was selected to ensure convergence of total energy and monkhorst-pack *k*-mesh with of 8*8*5 was employed for the *k*-space sampling of 2*2*1 supercell of Ca_2RuO_4 and $H_xCa_2RuO_4$. The DFT+*U* formula from Dudarev [8] was utilized to incorporate the Coulomb interaction *U*, with interaction parameters chosen as 3.0 eV for *U* and 0.3 eV for *J* according to the previous DFT+*U* studies for bulk ruthenates [9]. For spin-polarized (magnetic) DFT+*U* calculations, the total energy of ferromagnetic (FM), A-type (A-AFM) and G-type (G-AFM) anti-ferromagnetic orders are computed.

Supplementary Figures

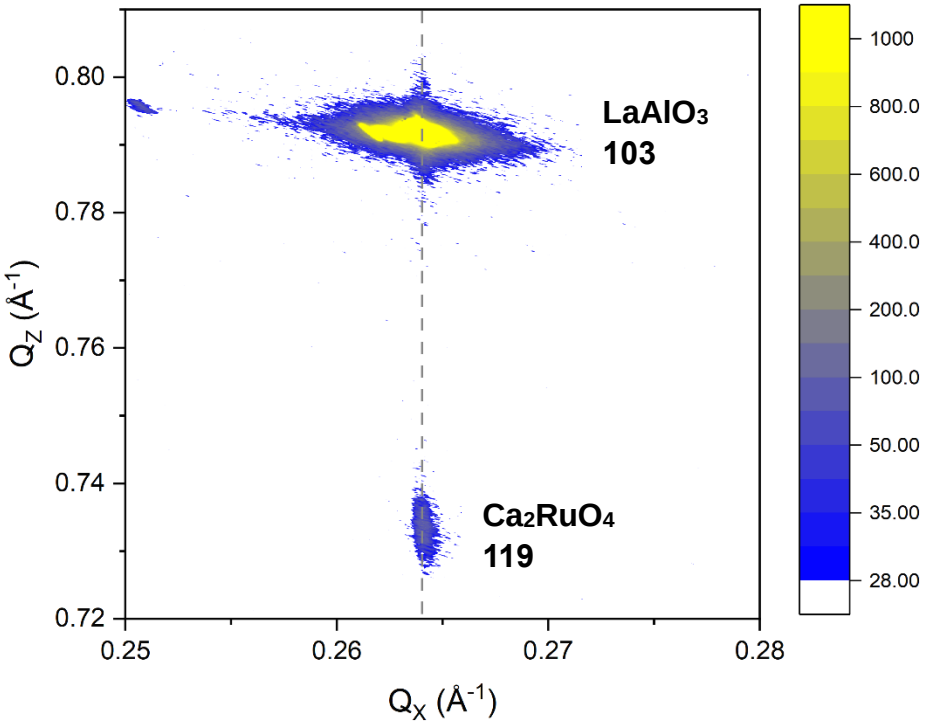

Fig. S1. X-ray reciprocal space mappings of Ca_2RuO_4 thin films grown on $LaAlO_3$ (001) substrates. As indicated by the dash line, the diffraction peak of the thin film appears at the same horizontal coordinate as that of the substrate, which indicates that the thin film is coherently strained to the substrate.

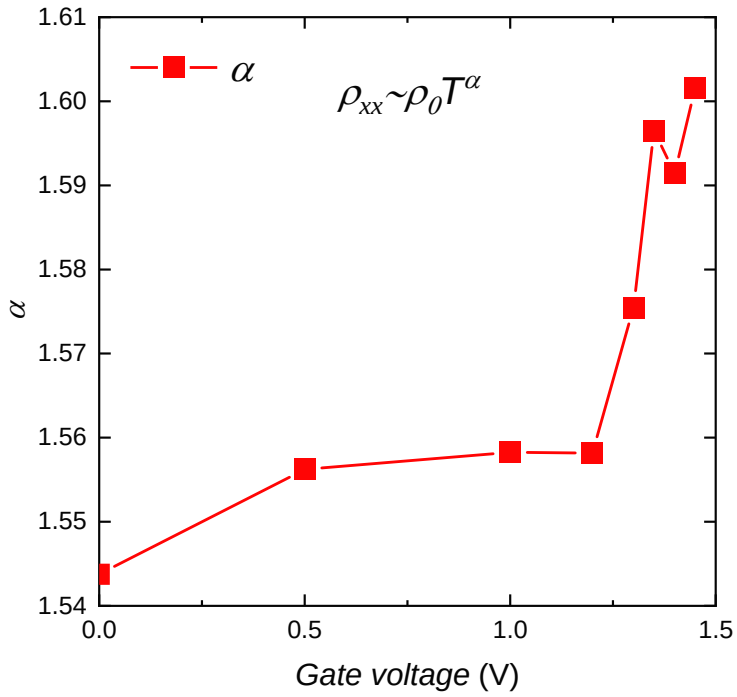

Fig. S2. Obtained fitting power law exponents (α) as a function of the gate voltage. The low temperature resistance data (below 8 K) were employed for gating voltages below 1.5 K, where the power law relationship of $\rho_{xx} \sim \rho_0 T^{\alpha}$ could nicely reproduce the data. The distinct deviation of α from 2 suggests a robust non-Fermi-liquid behavior of the observed metallic states.

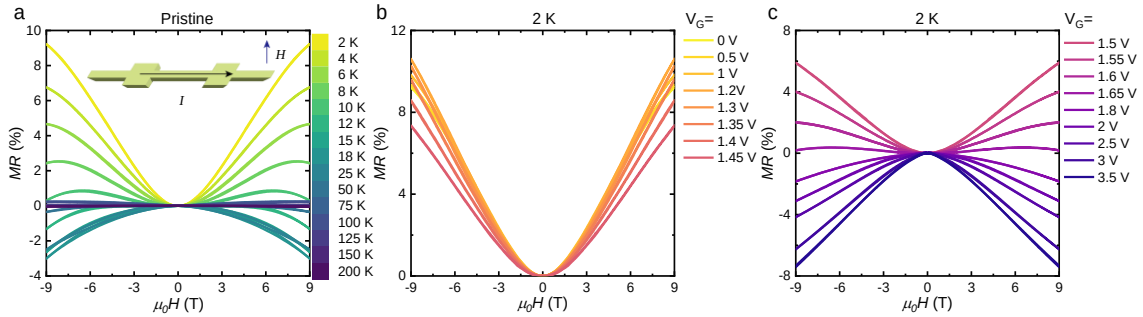

Fig. S3. Magnetoresistance (MR) data with the magnetic field ($\mu_0 H$) applied along the out-of-plane direction. (a) Field dependence of MR of the pristine Ca_2RuO_4 thin film at different temperatures. (b and c) Gating voltage dependent MR measured at 2 K for V_G below 1.5 V (b) and above 1.5 V (c). These data are similar to the in-plane MR, in which the MR changes sign from positive to negative at high V_G.

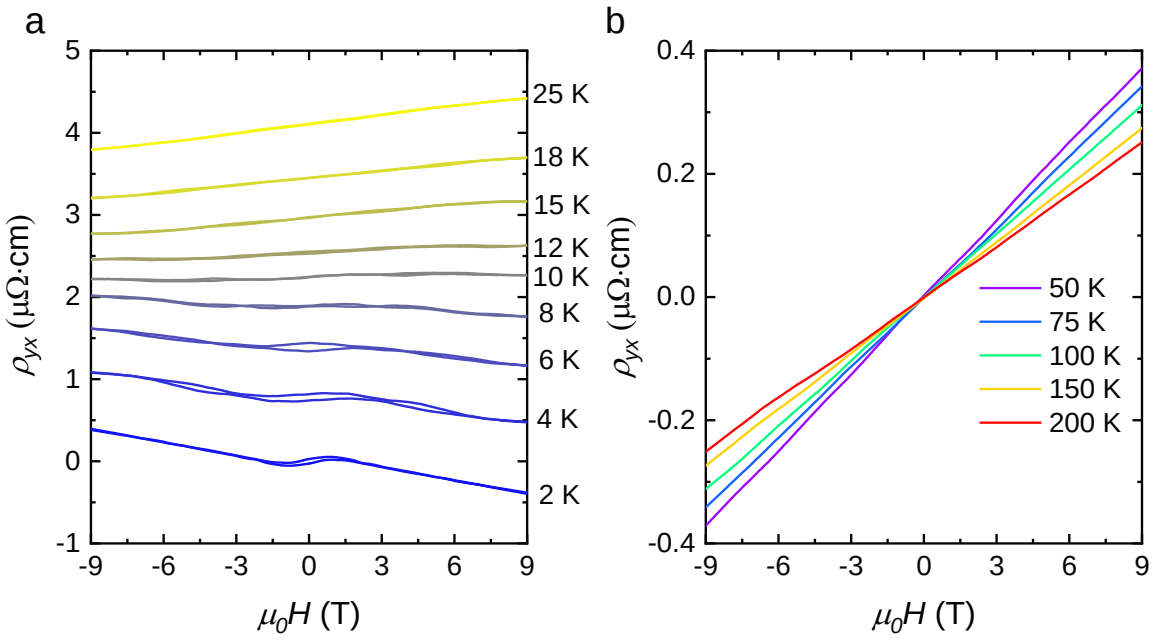

Fig. S4. Hall resistivity (ρ_{yx}) as a function of out-of-plane magnetic field ($\mu_0 H$) for the pristine Ca_2RuO_4 thin film at different temperatures.

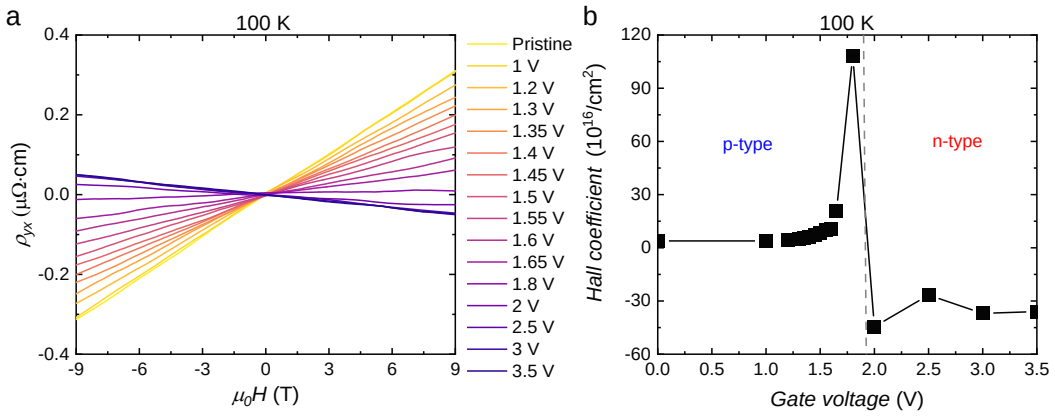

Fig. S5. Hall measurements at 100 K. (a) Hall resistivity (ρ_{yx}) as a function of the out-of-plane magnetic field ($\mu_0 H$) under different V_G. (b) Extracted Hall coefficients as a function of V_G. The dash line separates two regions dominated by p-type and n-type carriers, respectively.

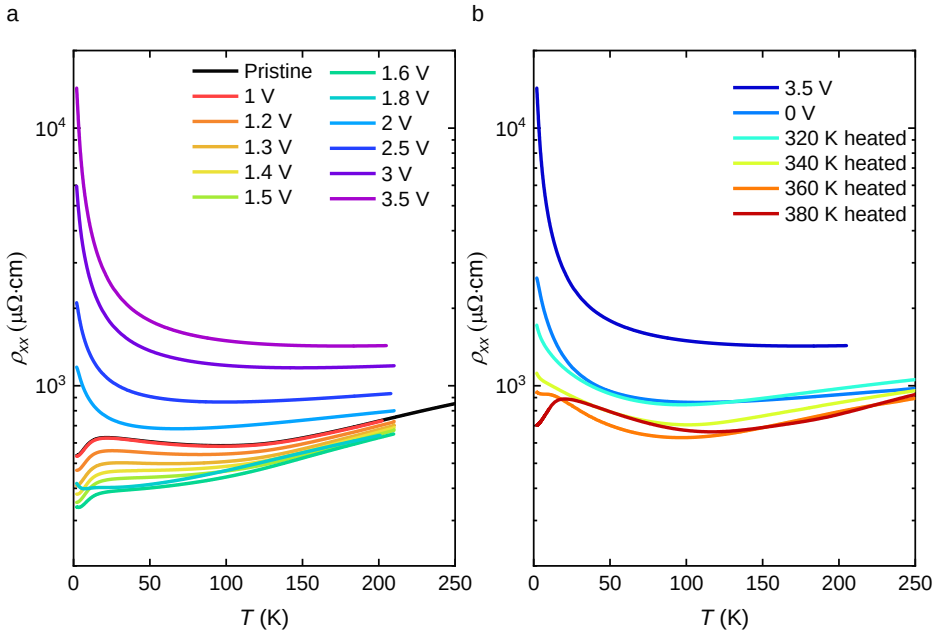

Fig. S6. Reversible evolution of ρ_{xx} through protonation. (a) Temperature dependence of resistivity ρ_{xx} at systematically increased gate voltage (V_G) up to 3.5 V. (b) evolution of ρ_{xx} upon heating in air after removing the gate voltage.

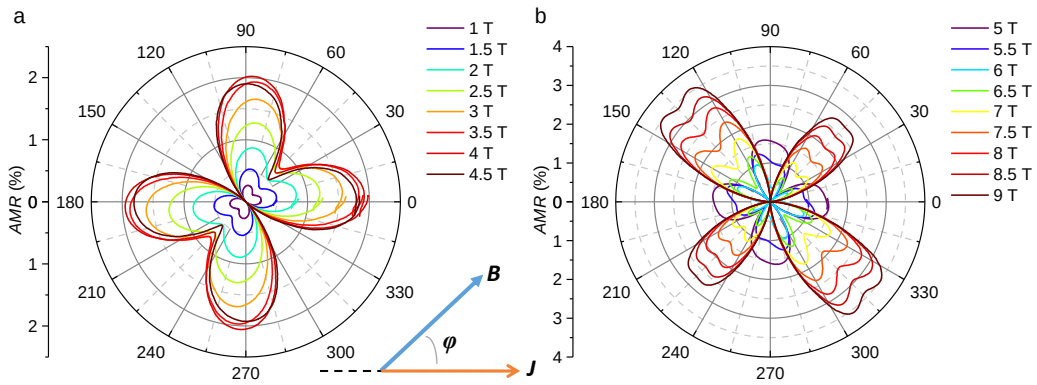

Fig. S7. Polar plots of in-plane AMR data under different magnetic fields ($\mu_0 H$) for the pristine Ca_2RuO_4 thin film, for the field below 4.5 T (a) and above 4.5 T (b), respectively. The data clearly reveal a transition in the shape of the AMR with increasing magnetic field.

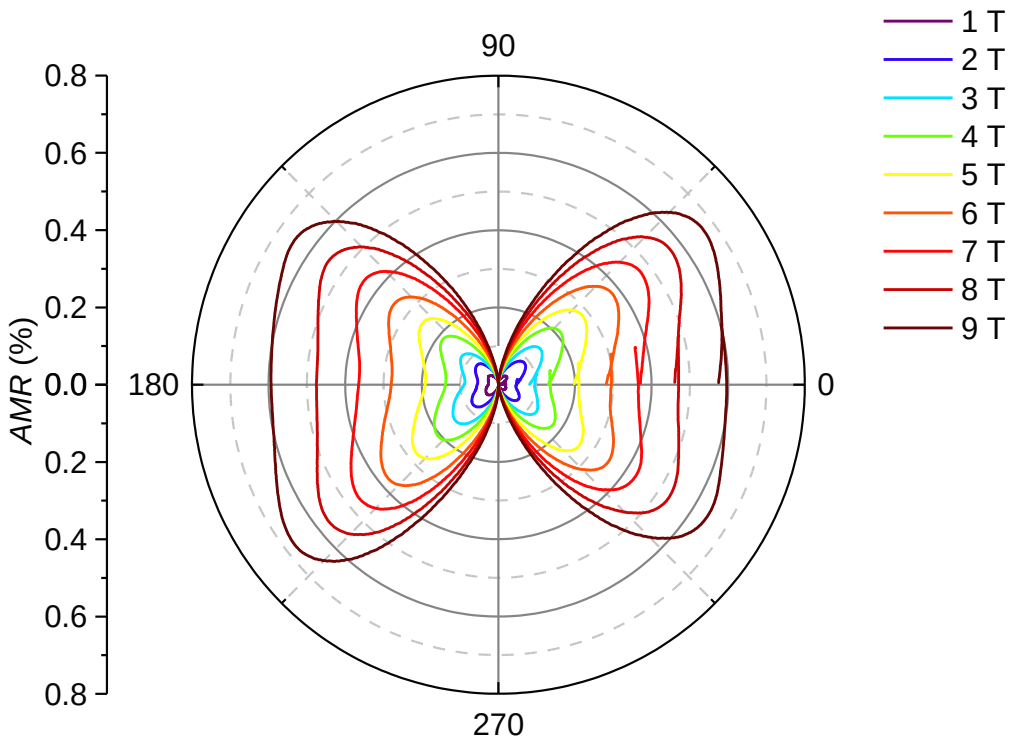

Fig. S8. Polar plots of in-plane AMR under different magnetic fields ($\mu_0 H$) for the gated (at 3.5 V) Ca_2RuO_4 thin film. These curves show an almost identical shape over the whole magnetic field range studied, which indicates the absence of a magnetic transition.

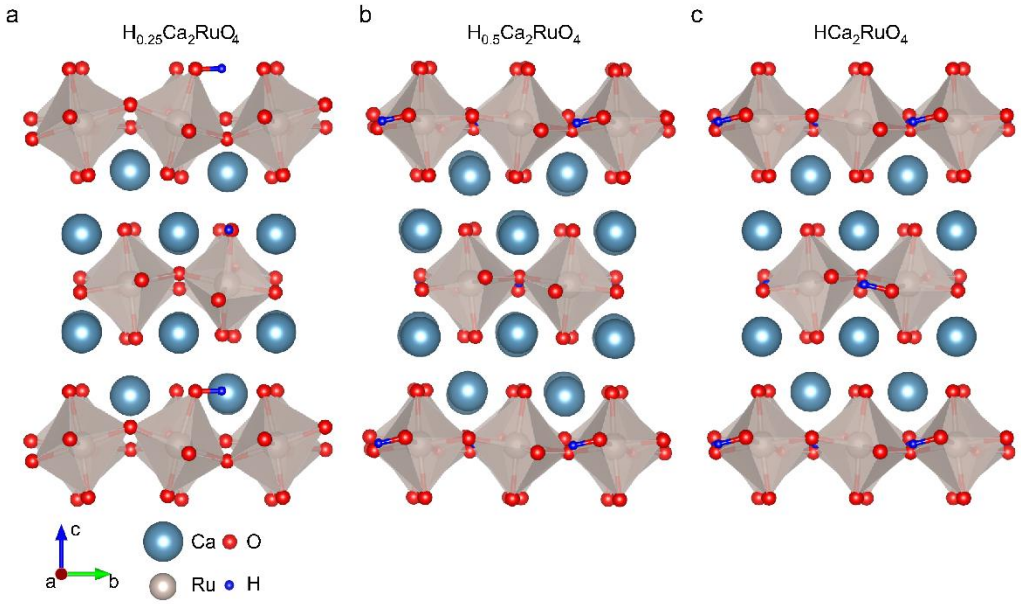

Fig. S9. Calculated lattice structures for $H_{0.25}Ca_2RuO_4$ (a), $H_{0.5}Ca_2RuO_4$ (b) and HCa_2RuO_4 (c).

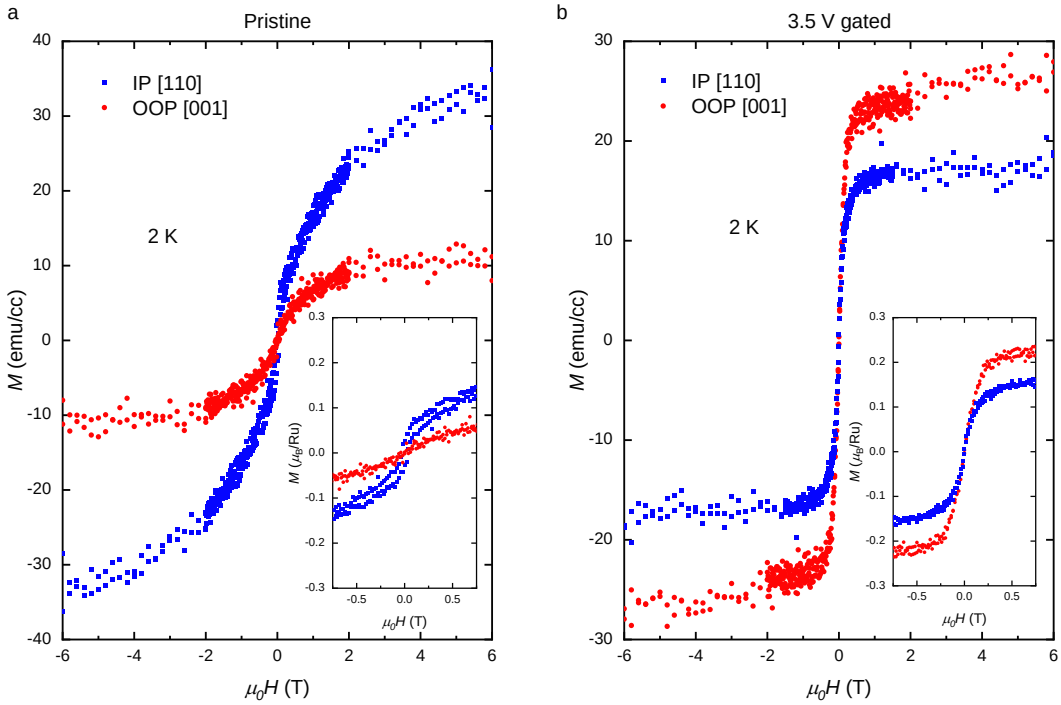

Fig. S10. Magnetism of pristine and hydrogenated Ca_2RuO_4. (a and b) In-plane (IP) and out-of-plane (OOP) magnetization measured along [110] and [001] directions, respectively, for both pristine (a) and 3.5 V gated (b) Ca_2RuO_4 films. The measurements were carried out at 2 K. The insets of (a) and (b) show the magnetization in units of μ_B/Ru at low fields.

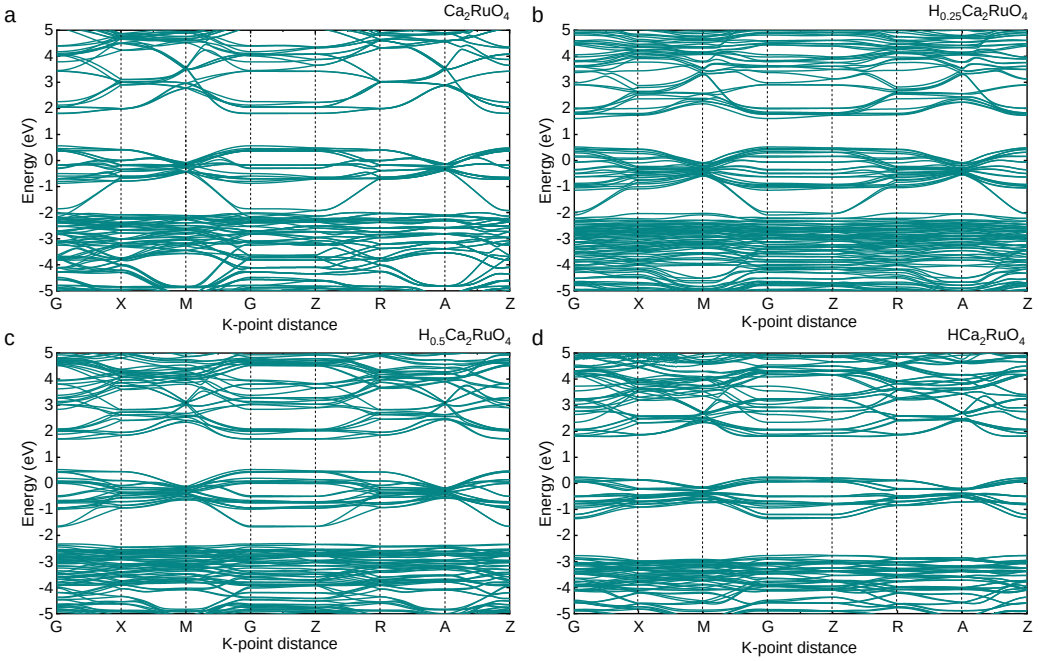

Fig. S11. Calculated non-spin-polarized Ru 4*d* band structures for Ca_2RuO_4 (a), $H_{0.25}Ca_2RuO_4$ (b), $H_{0.5}Ca_2RuO_4$ (c) and HCa_2RuO_4 (d) obtained from non-magnetic DFT calculations.

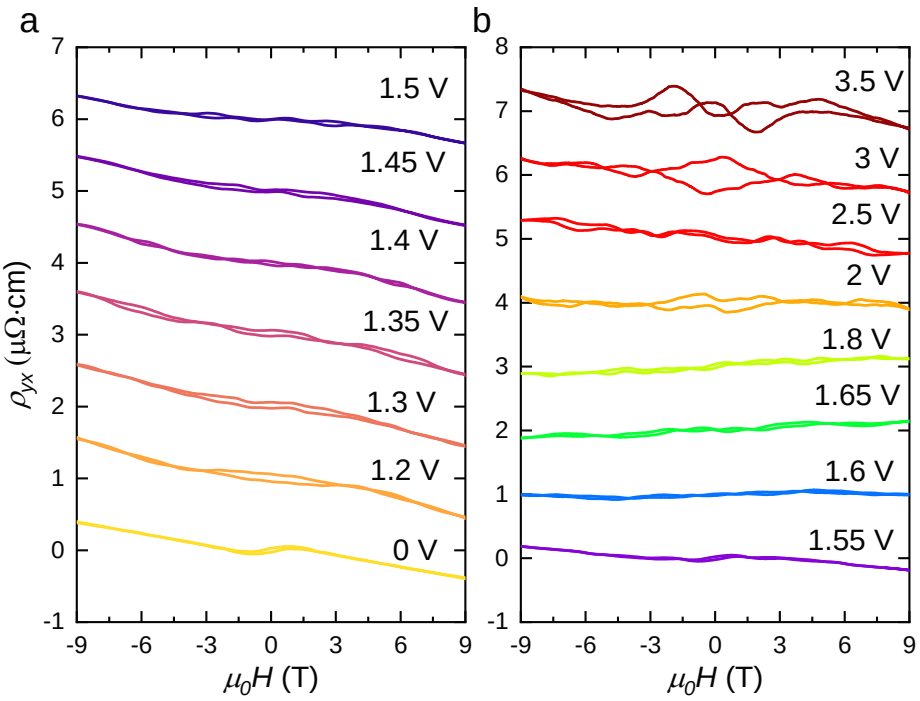

Fig. S12. Applied magnetic field ($\mu_0 H$) dependence of Hall resistivity (ρ_{yx}) at 2 K for different V_G. It is observed that the slope of the Hall resistivity changes sign from negative to positive at 1.65 V, then back into negative at 2 V. It is interesting to note that the Hall data show signatures of hysteresis, indicating the presence of long-range magnetic orders.

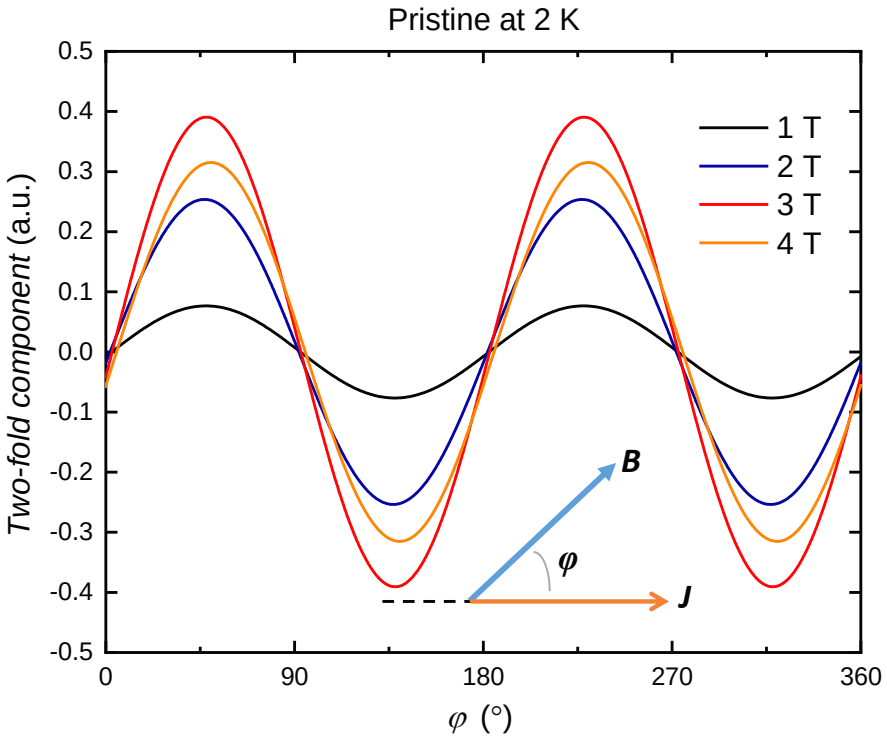

Fig. S13. Summary of the fitting results with 2-fold components for field-depended AMR results at pristine state. The data were obtained at 2 K under low magnetic fields ($\mu_0 H$) before the sample reaching metamagnetic transition. φ refers to the angle between the current and the in-plane magnetic field, as illustrated in the inset. It is seen that the maxima of these signals occur at angles of about 45° and 225° from the current, which can rule out the contribution of the Lorentz force, which should occur perpendicular to the direction of current flow.

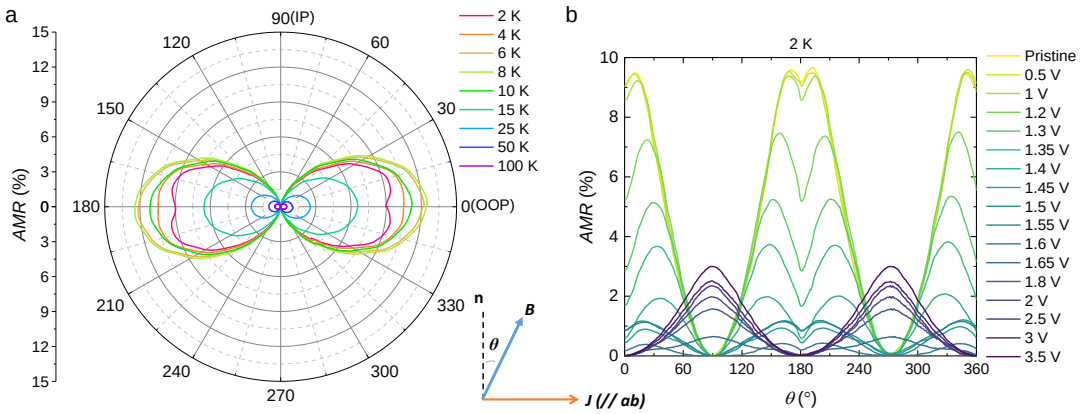

Fig. S14. Summary of AMR data as a function of the angle θ between the applied magnetic field ($\mu_0 H$) and thin film normal direction. In these measurements, θ = 0º and 90º correspond to the field applied along the out-of-plane and the in-plane directions, respectively. The magnetic field was set as 9 T for these measurements. (a) Polar plots of AMR for pristine Ca_2RuO_4 thin film at different temperatures. (b) Gating voltage dependent AMR obtained at 2 K. It is seen that the peak position is shifted for about 90º (from 0º to 90º) through the ILG.

Supplementary Tables

x	FM	A-AFM	G-AFM
0.0	64.8	62.4	**0.0**
0.25 (RuO_2)	2.3	1.7	0.0
0.25 (CaO)	-48.6	-48.5	**-85.3**
0.5 (RuO_2)	**-11.4**	**-11.4**	0.0
0.5 (CaO)	54.9	54.7	83.1
1.0 (RuO_2)	**-4.58**	**-4.57**	0.0
1.0 (CaO)	150.9	150.8	119.3

Table. S1. Calculated total energies of $H_xCa_2RuO_4$ at different hydrogen doping levels (x=0.0, 0.25, 0.5 and 1.0). For each H concentration, two possible crystal structures [RuO_2 layer (in-plane) occupation (injected protons form O-H bonds with the equatorial oxygens) and CaO layer (out-of-plane) occupation (injected protons form O-H bonds with the apical oxygens)] and three possible magnetic orders: ferromagnetic (FM), A-type antiferromagnetic (A-AFM), and G-type antiferromagnetic (G-AFM) are investigated. The energy of G-type AFM with in-plane hydrogen occupation is set as ground state for different doping levels. From this table, it is seen that the pristine Ca_2RuO_4 prefers G-AFM in the ground state. For the lightly doped sample ($H_{0.25}Ca_2RuO_4$), the G-AFM ground state is also preferred, in which the protons tend to be located in the CaO layer. Whereas for $H_{0.5}Ca_2RuO_4$ and HCa_2RuO_4 samples, the in-plane ferromagnetic coupling becomes dominant, and both FM and A-AFM orders become more energetically stable compared to the G-AFM.

	Ca_2RuO_4 (G-AFM)	HCa_2RuO_4 (A-AFM)	HCa_2RuO_4 (FM)
d_{xy} (spin up)	0.808	0.608	0.609
d_{xy} (spin down)	0.270	0.607	0.605
d_{yz} (spin up)	0.977	0.954	0.957
d_{yz} (spin down)	0.132	0.645	0.645
d_{xz} (spin up)	0.933	0.942	0.945
d_{xz} (spin down)	0.508	0.280	0.281
$d_{x^2-y^2}$ (spin up)	0.165	0.428	0.427
$d_{x^2-y^2}$ (spin down)	0.110	0.439	0.436
d_{z^2} (spin up)	0.062	0.070	0.071
d_{z^2} (spin down)	0.035	0.026	0.025
Total	4	5	5
Magnetic moment	1.890 μ_B	1.005 μ_B	1.019 μ_B

Table. S2. Calculated Ru 4*d* orbital occupation of the pristine Ca_2RuO_4 with G-type antiferromagnetic order, and HCa_2RuO_4 with both A-type antiferromagnetic (A-AFM) and ferromagnetic (FM) orders.

References

1. H. P. Nair *et al.*, Demystifying the growth of superconducting Sr2RuO4 thin films. *APL Materials* **6** (2018).
2. Hohenberg, Pierre, and Walter Kohn. Inhomogeneous electron gas. *Physical review* **136**(3B): B864-B871 (1964).
3. Kohn, Walter, and Lu Jeu Sham. Self-consistent equations including exchange and correlation effects. *Physical Review* **140**(4A): A1133-A1138 (1965).
4. Anisimov, Vladimir I., Jan Zaanen, and Ole K. Andersen. Band theory and Mott insulators: Hubbard U instead of Stoner I. *Physical Review B* **44**(3): 943-954 (1991).
5. Kresse, Georg, and Jürgen Furthmüller. Efficient iterative schemes for ab initio total-energy calculations using a plane-wave basis set. *Physical review B* **54**(16): 11169-11186 (1996).
6. Kresse, Georg, and Jürgen Furthmüller. Efficiency of ab-initio total energy calculations for metals and semiconductors using a plane-wave basis set. *Computational materials science* **6**(1): 15-50 (1996).
7. Perdew, John P., Kieron Burke, and Matthias Ernzerhof. Generalized gradient approximation made simple. *Phys Rev Lett* **77**(18): 3865-3868 (1996).
8. S. L. Dudarev, G. A. Botton, S. Y. Savrasov, C. J. Humphreys, and A. P. Sutton. Electron-energy-loss spectra and the structural stability of nickel oxide: An LSDA+ U study. *Physical Review B* **57**(3): 1505-1509 (1998).
9. L. Si, O. Janson, G. Li, Z. Zhong, Z. Liao, G. Koster, and K. Held. Quantum Anomalous Hall State in Ferromagnetic $SrRuO_3$ (111) Bilayers. *Phys Rev Lett* **119**, 026402 (2017).